Title

A trajectory mechanics approach for the study of wave propagation in an anisotropic elastic medium

Journal

Geophysical Journal International, 219(3)

ISSN

0956-540X

Authors

Vasco, DW
Nihei, Kurt T

Publication Date

2019-12-01

DOI

10.1093/gji/ggz406

Peer reviewed

Geophys. J. Int. (2019) **142,** 000–000

A trajectory mechanics approach for the study of wave propagation in an anisotropic elastic medium

D. W. Vasco and Kurt T. Nihei

Lawrence Berkeley National Laboratory,
University of California,
Berkeley, California 94720

Received 2019; in original form 2019 April

SUMMARY

We derive equations describing the path and travel time of a coherent elastic wave propagating in an anisotropic medium, generalizing expressions from conventional high-frequency asymptotic ray theory. The methodology is valid across a broad range of frequencies and allows for sub-wavelength variations in the material properties of the medium. The primary difference from current ray methods is the retention of a term that is neglected in the derivation of the eikonal equation. The additional term contains spatial derivatives of the properties of the medium and of the amplitude field, and its presence couples the equations governing the evolution of the amplitude and phase along the trajectory. The magnitude of this term provides a measure of the validity of expressions based upon high-frequency asymptotic methods, such as the eikonal equation, when modeling wave propagation dominated by a band of frequencies. In calculations involving a layer with gradational boundaries, we find that asymptotic estimates do deviate from those of our frequency-dependent approach when the width of the layer boundaries become sufficiently narrow. For example, for a layer with boundaries that vary over tens of meters, the term neglected by a high-frequency asymptotic approximation is significant for frequencies around 10 Hz. The visible differences in the paths of the rays that traverse the layer substantiate this conclusion. For a velocity model derived from an observed well log, the majority of the trajectories calculated using the extended approach, accounting for the frequency-dependence of the rays, are noticibly different from those produced by the eikonal equation. A suite of paths from a source to a specified receiver, calculated for a range of frequencies between 10 and 100 Hz, define a region of sensitivity to velocity variations and may be used for an augmented form of tomographic imaging.

Key words: Seismic wave propagation, anisotropy, seismic tomography, seismic imaging, ray methods for anisotropic media.

1 INTRODUCTION

The importance of anisotropy has become increasingly evident for a wide range of geophysical applications. It has been known for some time that anisotropy can severely impact seismic imaging in sedimentary basins containing shale, motivating interest in techniques for migration and modeling in such media (Tsvankin 2012). More recently, hydraulic fracturing in shale formations has generated additional interest in modeling wave propagation in anisotropic material in order to locate microseismic events and to invert for anisotropic velocities (Grechka et al. 2011, Li et al. 2014). Anisotropy due to the presence of fractures and the nonlinear response of rocks to stress is well established and documented by numerous studies (e.g. Thurston and Brugger 1964, Nur 1971, Sayers and Kachanov 1995, Mavko et al. 1995, Sarkar et al. 2003). Thus, seismic anisotropy can be indicative of the stress state of a rock and changes in anisotropy may be a sign of changes in the state of stress (Sayers 2010).

Due to the complexity of modeling elastic wave propagation in a heterogeneous anisotropic medium, it is desirable to have flexible methods for forward modeling, visualization, and imaging. Numerical methods, such as finite-differences, are the most general and, with sufficiently dense griding, can be accurate and stable (Robertsson et al. 2012, Car-

cione 2014). However, even with current parallel computers, such approaches can require long simulation times in order to solve the forward problem and much more time to solve the inverse problem. There are statistical approaches that consider wave propagation through a random distribution of scatters (Ishimaru 1997, Coates and Chapman 2007, Sato et al. 2012). For a coherent medium with known boundaries ray methods are an alternative approach that provide insight through semi-analytic expressions for, and visualization of, the propagation path in an anisotropic medium (Aki and Richards 2002, p. 82). Such techniques have a long history and scale well with problem size (Vlaar 1968, Cerveny 1972, Cerveny et al. 1977, Gajewski and Psencik 1987, 1990, Shearer and Chapman 1989, Vavrycuk 2001, Cardarelli and Cerreto 2002, Chapman 2004, Zhang et al. 2017, Gou et al. 2018) but can be difficult to implement and have convergence issues in complicated models. More importantly, high-frequency asymptotic ray theory may not accurately model wave propagation at all frequencies of interest, particularly in the presence of rapidly-varying properties such as narrow transition zones.

Here we extend the trajectory mechanics approach introduced by Vasco and Nihei (2019) to an elastic medium with anisotropic properties. That approach, adopted from techniques used in quantum dynamics (Bohm 1952, Takabayasi 1952, Bohm 1989, Wyatt 2005, Benseny et al. 2014, Gu and Garashchuk 2016), retains terms that are neglected in the high-frequency approximations used in asymptotic ray methods (Chapman 2004) and in the eikonal equation (Faria and Stoffa 1999, Brantut 2018). We present the technique as an adjunct to existing numerical methods, providing flexibility in forward and inverse modeling. The semi-analytic expressions provide some insight into the factors governing propagation paths. Furthermore, the trajectories may be used to visualize wave propagation in a complicated medium and to construct semi-analytic sensitivities for efficient imaging (Vasco 2018, Vasco and Nihei 2019). A related approach was developed by Foreman (1989) for computing trajectories associated with propagation governed by the scalar Helmholtz equation, independently of the work in quantum mechanics. The technique was recently applied to construct frequency-dependent rays for several numerical examples (Protasov and Gadylshin 2017). A data analysis and imaging procedure known as Helmholtz tomography, based upon similar ideas, was applied to surface wave observations by Lin and Ritzwoller (2011) and used for the study of building vibrations by Kohler et al. (2018). Our work, and that presented in Vasco and Nihei (2019), can be considered as an extension of the work of Foreman (1989, as well as a generalization of related efforts in quantum mechanics and physics (Orefice et al. 2009), to the full vector elastodynamic equations of motion. Furthermore, whereas the approach of Foreman (1989) and Protasov and Gadylshin (2017) requires the solution of the governing Helmholtz equation, we derive a trajectory-based set of ordinary differential equations that may be solved in place of the full governing partial differential equations. Such an approach has been shown to be more efficient for the calculation of trajectories associated with quantum dynamics (Wyatt 2005).

The techniques that we present provide a connection between travel time sensitivity kernels computed using numerical wave propagation codes and conventional ray methods. It has been pointed out that the sensitivity kernels associated with travel times obtained from band-limited waveforms are actually averaging volumes with some finite width (Weilandt 1987, Luo and Schuster 1991, Woodward 1992, Cerveny and Soares 1992, Stark and Nikolayev 1993, Lomax 1994, Vasco et al. 1995, Zelt and Chen 2016). For travel times obtained from waveform cross-correlations Luo (1991) and Vasco and Majer (1993) were the first to derive travel time sensitivity functions using the adjoint approach developed by Tarantola (1984, 1988) for seismic waveform inversion. Their method was subsequently adopted by Marquering et al. (1999) and used by many others for seismic tomographic investigations [see Koroni et al. (2019) for a recent study]. As discussed below, one may use the trajectories derived here to construct extended regions between a given source-receiver pair that are sensitive to the propagation of a range of specific frequency components of the wave field. In that way, the band-limited nature of the wave field can be accounted for in constructing a tomographic image. Furthermore, the method can serve as the basis for frequency-dependent tomographic imaging, with a number of potential applications, such as the imaging of fluid-related time-lapse changes.

2 METHODOLOGY

2.1 Governing Equations

In treating the anisotropic equation of motion it is important to adopt a succinct notation in order to avoid a proliferation of indices. For example, the basic constitutive relation for a general elastic and anisotropic solid, provides a linear relationship between the strain tensor e_{kl} and the stress tensor σ_{ij} and is given in its most general form as

$$\sigma_{ij} = c_{ijkl} e_{kl}, \tag{1}$$

where the indices run from 1 to 3 and we employ Einstein's convention of summing over repeated indices. We shall use the notation of Woodhouse (1974) and Chapman (2004), combining bold font vector-tensor notation with a reduced use of indices. In their notation we represent some higher-order tensors as indexed lower-order quantities. For example, the stress tensor is given by three indexed column vectors, $\mathbf{t}_j$ for $j = 1, 2, 3$, and where the i-th component of the j-th vector gives the ij component of the stress tensor

$$(\mathbf{t}_j)_i = \sigma_{ij}. \tag{2}$$

The fourth-order tensor $c_{ijkl}(\mathbf{x})$ relating stress and strain in equation (1) is represented as a indexed set of 3×3 matrices

$$c_{ijkl} = (\mathbf{c}_{jk})_{il}\,. \tag{3}$$

The hybrid notation allows us to write the equation governing the propagation of an elastic disturbance in an anisotropic medium in a rather compact form

$$\rho \frac{\partial^2 \mathbf{u}}{\partial t^2} = \frac{\partial \mathbf{t}_j}{\partial x_j} + \mathbf{f}, \tag{4}$$

with displacements given by the vector $\mathbf{u}(\mathbf{x}, t)$, and where $\mathbf{f}(\mathbf{x}, t)$ is a source or body force and $\rho(\mathbf{x})$ is the density, along with the constitutive relationship

$$\mathbf{t}_j = \mathbf{c}_{jk} \frac{\partial \mathbf{u}}{\partial x_k}, \tag{5}$$

relating stress and strain. Applying the Fourier transform maps these two equations into the frequency domain and the displacement and stress vectors map into $\mathbf{U}(\mathbf{x},\omega)$ and $\mathbf{T}(\mathbf{x},\omega)$, respectively. Substituting the constitutive relationship into the governing equation results in the single equation

$$-\omega^2\rho\mathbf{U} = \frac{\partial}{\partial x_j}\left[\mathbf{c}_{jk}\frac{\partial \mathbf{U}}{\partial x_k}\right] \tag{6}$$

for the displacement vector $\mathbf{U}(\mathbf{x},\omega)$ in terms of the frequency ω, where we are summing over j and k. Since we are modeling the propagating wave field, it is assumed that we are away from the source and its direct influence.

We are interested in modeling the propagation of a coherent body wave, so we assume that the three components of displacement at a point are all due to a passing wavefront. Therefore, away from known boundaries, we write the complex displacement vector in the polar form, a generalization of a plane wave decomposition in which both the phase and amplitude depend upon ω,

$$\mathbf{U}(\mathbf{x},\omega) = \mathbf{R}(\mathbf{x},\omega)e^{i\varphi(\mathbf{x},\omega)} \tag{7}$$

where both the components of the amplitude vector $\mathbf{R}(\mathbf{x},\omega)$ and the scalar phase function $\varphi(\mathbf{x},\omega)$ are real valued. In adopting this form of the solution we are neglecting the back-propagating wave fields and conversions to interface waves that might be introduced by the scattering off of discontinuities. Note that the wave field (7) has a general frequency dependence leading to quantities, such as ray paths, that depend upon ω.

A semi-analytical trajectory-based solution follows if we substitute the form (7) into the governing equation (6). As shown in the Appendix, the resulting equation contains real and imaginary terms. Setting the two equations defined by each set of terms to zero produces two coupled equations in φ and $\mathbf{R}$. These equations define the trajectory upon which the solution is calculated and the evolution of the amplitude along the trajectory. In the sub-sections that follow we consider these equations and demonstrate how they lead to a solution that is define along trajectories or paths through the anisotropic medium.

2.2 Real Terms and the equations defining the trajectory

2.2.1 An Expression for the Hamiltonian

As shown in the Appendix, if we consider just the real terms that result when the polar form (7) is substituted into equation (6) we arrive at the matrix equation

$$\left[\mathbf{a}_{jk}\frac{\partial\varphi}{\partial x_k}\frac{\partial\varphi}{\partial x_j} - \omega^2\mathbf{I}\right]\mathbf{R} = \frac{1}{\rho}\frac{\partial}{\partial x_j}\left(\rho\mathbf{a}_{jk}\frac{\partial\mathbf{R}}{\partial x_k}\right), \tag{8}$$

see equation (A6) in the Appendix, where we have defined the density-normalized anisotropy coefficients $\mathbf{a}_{jk}(\mathbf{x})$ by

$$\mathbf{a}_{jk} = \frac{1}{\rho}\mathbf{c}_{jk}, \tag{9}$$

and the quantity $\mathbf{I}$ represents the identity matrix. Equation (8) resembles the eikonal equation for the phase found in high-frequency asymptotic ray theory (Cerveny 1972, Chapman 2004, p. 164). In fact, if we can neglect the right-hand-sides of equation (8), either because ω is sufficiently large and/or the spatial gradients of $\mathbf{a}_{jk}$ and $\mathbf{R}$ are small, then the coupling between the phase, contained in terms on the left-hand-side, and the amplitude disappears. We can use the condition for a non-trivial solution for $\mathbf{R}$, given by the vanishing of the determinant of the coefficient matrix in brackets in equation (8)

$$\det\left[\mathbf{a}_{jk}\frac{\partial\varphi}{\partial x_k}\frac{\partial\varphi}{\partial x_j} - \rho\omega^2\mathbf{I}\right] = 0, \tag{10}$$

to solve for the phase φ directly.

In general, the right-hand-side of equation (8) cannot be neglected and one must treat the full expression, as we now demonstrate. First, we can recast equation (8) in terms of the slowness vector, which is defined as

$$\mathbf{p}(\mathbf{x},\omega) = \frac{1}{\omega}\mathbf{k}(\mathbf{x},\omega) = \frac{1}{\omega}\nabla\varphi, \tag{11}$$

where $\mathbf{k}(\mathbf{x},\omega)$ is the wave number vector. Substituting for $\nabla\varphi$ in equation (8) produces a quadratic equation in the components of the slowness vector

$$\left[\mathbf{a}_{jk}p_jp_k - \mathbf{I}\right]\mathbf{R} = \mathbf{W}, \tag{12}$$

where we have defined the vector

$$\mathbf{W}(\mathbf{x},\omega) = \frac{1}{\omega^2\rho}\frac{\partial}{\partial x_j}\left(\rho\mathbf{a}_{jk}\frac{\partial\mathbf{R}}{\partial x_k}\right) \tag{13}$$

in terms of the right-hand-side of equation (8) normalized by ω^2. Re-arranging equation (12) and multiplying both sides by $\mathbf{R}^t$ we can define

$$E(\mathbf{x},\omega) = \mathbf{R}^t\mathbf{a}_{jk}p_jp_k\mathbf{R} - \mathbf{R}^t\mathbf{W} = R^2, \tag{14}$$

were $R(\mathbf{x},\omega)$ is the amplitude of the displacement vector $\mathbf{R}$. Thus, $E(\mathbf{x},\omega)$ is a measure of the energy of the elastic disturbance. Given that $\mathbf{W}$ is a linear operator applied to $\mathbf{R}$, we observe that $E(\mathbf{x},\omega)$ is a quadratic form in terms of the displacement amplitude vector $\mathbf{R}$. The function $E(\mathbf{x},\omega)$ has an implicit dependence upon the spatial coordinates $\mathbf{x}$. Typically ω is taken to be a parameter rather than an independent variable and we consider the frequency to be fixed at a particular value.

Central to the investigation of any physical system is the definition of a Hamiltonian function, as it determines the corresponding dynamics. The Hamiltonian function is particularly important in the calculation of trajectories associated with the propagation of transient disturbances and wavefronts. A useful definition of the Hamiltonian follows directly from equation (14), after dividing through by R^2

$$H(\mathbf{x},\mathbf{p},\omega) = \hat{\mathbf{R}}^t\mathbf{a}_{jk}p_jp_k\hat{\mathbf{R}} - W \tag{15}$$

where the function $W(\mathbf{x},\omega)$ is the component of the vector $\mathbf{W}$ in the direction of the amplitude vector $\mathbf{R}$

$$W(\mathbf{x},\omega) = \frac{1}{R}\hat{\mathbf{R}}^t\mathbf{W}. \tag{16}$$

Note that in the definition of the Hamiltonian we are treating $\mathbf{p}$ as an independent variable. Equation (14) corresponds to the constraint that the Hamiltonian for the elastic system is a constant, that is

$$H(\mathbf{x},\mathbf{p},\omega) = 1, \tag{17}$$

given our normalization by R^2. Due to the presence of W, the phase does not decouple from the amplitude in a medium with rapid spatial variations in properties, unlike the Hamiltonian in asymptotic ray theory.

2.2.2 Equations for the trajectory

Using methods from the theory of partial differential equations one can derive an equivalent set of ordinary equations defined along trajectories (Courant and Hilbert 1966). An intuitive argument follows if we consider a solution defined along a trajectory $\mathbf{x}(T)$, where T signifies position along the path, in this case in terms of the travel time to a point on the path. Both variables $\mathbf{x}$ and $\mathbf{p}$ are considered functions of T while ω remains a fixed parameter. If we differentiate equation (17) with respect to T, making use of the fact that H is constant along the trajectory, we find that

$$\frac{dH}{dT} = \nabla_x H \cdot \frac{d\mathbf{x}}{dT} + \nabla_p H \cdot \frac{d\mathbf{p}}{dT} = 0. \tag{18}$$

One can consider equation (18) to be a condition for the orthogonality of two vectors that is satisfied if

$$\frac{dx_j}{dT} = \frac{1}{2}\frac{\partial H}{\partial p_j} \tag{19}$$

$$\frac{dp_j}{dT} = -\frac{1}{2}\frac{\partial H}{\partial x_j} \tag{20}$$

where, because the condition for orthogonality is not sensitive to the magnitude of the vectors, we have scaled one of the vectors by 1/2. This results in expressions that are of the same form as in Gajewski and Psencik (1987) and Chapman and Pratt (1992). Furthermore, it will eliminate a non-essential factor of 2 that would otherwise appear in later travel time calculations. This is equivalent to multiplying equation (18) by a factor of 1/2. For the Hamiltonian given by equation (17) these ordinary differential equations take the form

$$\frac{dx_j}{dT} = \hat{\mathbf{R}}^t \mathbf{a}_{jm} \hat{\mathbf{R}} p_m = V_j \tag{21}$$

$$\frac{dp_j}{dT} = -\frac{1}{2}\frac{\partial}{\partial x_j}\left[\hat{\mathbf{R}}^t \mathbf{a}_{lm} \hat{\mathbf{R}}\right] p_l p_m + \frac{1}{2}\frac{\partial W}{\partial x_j} \tag{22}$$

for $j = 1, 2, 3$, where V_j is the j-th component of the group velocity vector $\mathbf{V}$. We are assuming that $\mathbf{R}(\mathbf{x}, \omega)$ only depends upon position and frequency and does not have a dependence upon $\mathbf{p}$. Note that the trajectory depends strongly on the wave field orientation through the presence of $\hat{\mathbf{R}}$ in equation (21). In addition, the paths are influenced by the spatial variations in the material properties and the wave field amplitudes due to the term containing W in equation (22). Equation (21) is similar in character to that found in the ray theory of Vlaar (1968) based upon the propagation of discontinuities, and in asymptotic ray theory (Gajewski and Psencik 1987).

2.2.3 Propagation of compressional (qP) and shear phases (qS)

Up to this point we have not distinguished between the various modes of elastic wave propagation, that is between compressional and shear waves. This makes some sense because the modes do couple in the presence of rapidly-varying heterogeneity. However, at any given location, one can make use of the symmetry of the matrix on the left-hand-side of equation (12) to deduce that there are generally three modes of propagation with differing velocities. In particular, note that the first term in equation (12), denoted by

$$\mathbf{\Gamma} = \mathbf{a}_{jk} p_j p_k, \tag{23}$$

is a real symmetric 3×3 matrix that has the eigendecomposition

$$\mathbf{\Gamma} = \mathbf{G} \mathbf{\Lambda} \mathbf{G}^t \tag{24}$$

(Strang 2016) where the columns of the matrix $\mathbf{G}$ constitute a set of three orthonormal vectors that we denote by $\hat{\mathbf{g}}_i, i = 1, 2, 3$, and $\mathbf{\Lambda}$ is a diagonal matrix. The vectors $\hat{\mathbf{g}}_i$ are the polarization directions of coherent waves propagating in the anisotropic medium passed a particular point. The polarization directions, defining the three modes of propagation, are the solutions of the eigenvalue problem

$$\mathbf{a}_{jk} p_j p_k \hat{\mathbf{g}}_i = \lambda_i \hat{\mathbf{g}}_i, \tag{25}$$

(Chapman 2004, p. 164). The diagonal elements of $\mathbf{\Lambda}$ are eigenvalues of the matrix $\mathbf{\Gamma}$, given by the solutions of the cubic equation

$$\det\left[\mathbf{a}_{jk} p_j p_k - \lambda \mathbf{I}\right] = 0, \tag{26}$$

that follows from the condition that a non-trivial solution of equation (25) exists.

One can use equation (25) to interpret the eigenvalues in terms of the slowness, or phase velocity, of a propagating elastic wave in the given anisotropic medium. First, let us fix the direction of the phase velocity vector $\mathbf{p}$ and define the magnitude of the vector, the slowness s, and its reciprocal the phase velocity v,

$$\mathbf{p} = s\hat{\mathbf{p}} = \frac{1}{v}\hat{\mathbf{p}} \tag{27}$$

where $\hat{\mathbf{p}}$ is a unit vector in the direction of the phase velocity vector. Pre-multiplying equation (25) by $\hat{\mathbf{g}}$ and making use of the definition (27) gives

$$v = \sqrt{\frac{\hat{\mathbf{g}}_i^t \mathbf{a}_{jk} \hat{\mathbf{g}}_i \hat{p}_j \hat{p}_k}{\lambda_i}}. \tag{28}$$

For a specific location and a fixed direction, $\hat{\mathbf{p}}$, the eigenvalue λ_i determines the phase velocity of the i-th mode of propagation with polarization vector $\mathbf{g}_i$.

It is evident from equation (28) that the mode associated with the smallest eigenvalue has the largest phase velocity and will likely be the first observed phase at a particular receiver. By analogy with asymptotic ray theory (Cerveny 1972, Gajewski and Psencik 1987, Chapman 2004) we refer to this mode as the quasi-compressional, or the quasi-P, phase and use the subscript qP to designate quantities associated with it. Note that the qP phase maps to the compressional wave in isotropic wave propagation as the anisotropy is reduced to zero. In addition, there are the two later arriving quasi-shear phases signified as qS_1 and qS_2. Note that is many situations, such as an isotropic medium the shear modes will not be distinguishable and the decomposition is degenerate because there are effectively only two phases.

In our applications we shall focus on observations corresponding to phases that have propagated solely as quasi-P waves, as these are the first arriving signals and it is much easier to identify them and to pick their onsets. Furthermore, they rarely suffer from the potential degeneracies associated with the later arriving quasi-S or quasi-shear waves that can make their interpretation difficult (Jech 1991). For applications such as transmission tomography and locating

earthquakes we will be interested in phases that have propagated from a given source to an observation point solely as quasi-P waves, the direct P wave. For such waves the amplitude vector is aligned along the polarization direction $\hat{\mathbf{g}}_{qP}$ associated with the smallest eigenvalue λ_{qP}. Thus, the Hamiltonian can be cast in terms of the polarization vector

$$H(\mathbf{x},\mathbf{p}) = \hat{\mathbf{g}}_{qP}^t \mathbf{a}_{jk} \hat{\mathbf{g}}_{qP} p_j p_k - W(\mathbf{x},\omega). \tag{29}$$

The group velocity for this phase is obtained from the ray equation (21) and the j-th component is given by

$$\left(\mathbf{V}_{qP}\right)_j = \hat{\mathbf{g}}_{qP}^t \mathbf{a}_{jm} \hat{\mathbf{g}}_{qP} p_m, \tag{30}$$

and the phase velocity is obtained from equation (28) with the appropriate substitutions

$$v = \sqrt{\frac{\hat{\mathbf{g}}_{qP}^t \mathbf{a}_{jk} \hat{\mathbf{g}}_{qP} \hat{p}_j \hat{p}_k}{\lambda_{qP}}}, \tag{31}$$

where λ_{qP} is the smallest eigenvalue associated with the quasi-compressional wave. Similar expressions are used to calculate the group velocity of the later arriving quasi-Shear phases identified with the two largest eigenvalues, denoted by λ_{qS_1} and λ_{qS_2}. For example, the group velocity for the phase qS_1 is found using the expression

$$\left(\mathbf{V}_{qS_1}\right)_j = \hat{\mathbf{g}}_{qS_1}^t \mathbf{a}_{jm} \hat{\mathbf{g}}_{qS_1} p_m. \tag{32}$$

2.3 Imaginary terms and energy transport along a trajectory

As shown in the Appendix, the imaginary terms obtained after substituting the polar form of the displacement vector (7) into the governing equation (6) provides a second linear partial differential equation that we may write in terms of the slowness vector $\mathbf{p}$

$$\frac{\partial}{\partial x_j}\left[p_k \mathbf{c}_{jk} \mathbf{R}\right] + p_j \mathbf{c}_{jk} \frac{\partial \mathbf{R}}{\partial x_k} = 0. \tag{33}$$

This transport equation, governing the flow of energy of the propagating wave, is of the same form as the expression provided by a high-frequency asymptotic analysis (Gajewski and Psencik 1987). In particular, the left-hand-side of equation (34) is identical to the operator $M(\mathbf{R})$ defined by Cerveny et al. (1977, p. 160) and Chapman (2004, p. 164). In order to maintain compatibility with the expressions given above, we rewrite equation (33) in terms of $\mathbf{a}_{jk}$ given by equation (9)

$$M(\mathbf{R}) = \frac{\partial}{\partial x_j}\left[p_k \rho \mathbf{a}_{jk} \mathbf{R}\right] + p_j \rho \mathbf{a}_{jk} \frac{\partial \mathbf{R}}{\partial x_k} = 0. \tag{34}$$

For a given slowness field equation (34) is a linear partial differential equation that accounts for such effects as geometrical spreading. Here we are considering both $\mathbf{p}$ and $\mathbf{R}$ to be dependent variables, and hence equations (12) and (34) must be treated as nonlinear coupled equations. Because the slowness vectors can differ from those calculated using an asymptotic approach, the amplitude estimates provided by equation (34) will likewise differ. As noted in Vlaar (1968) and others [for example Cerveny et al. (1977) and Chapman 2004], it is possible to write the partial differential equation (34) in ray coordinates, with one axis along $\mathbf{x}(s)$. To this end, if we consider the quasi-compressional wave, we can write the amplitude vector in the form

$$\mathbf{R} = R_{qP} \hat{\mathbf{g}}_{qP} + \mathbf{R}_\perp \tag{35}$$

where R_{qP} is the amplitude function in the direction of the polarization vector corresponding to the quasi-compressional mode and $\mathbf{R}_\perp$ is the component perpendicular to this mode. As noted in Chapman (2004, p. 171), multiplying on the left by $\hat{\mathbf{g}}_{qP}^t$ produces the equation

$$\hat{\mathbf{g}}_{qP}^t M(\mathbf{R}) = 0. \tag{36}$$

Because equation (36) has been reduced to a scalar we can transpose the second term in equation (34) and multiply by R_{qP} to arrive at a transport equation in canonical form

$$\nabla \cdot \left(\rho R_{qP}^2 \mathbf{V}_{qP}\right) = 0 \tag{37}$$

where $\mathbf{V}_{qP}$ is the group velocity defined earlier [see equation (30)]. Carrying out the differentiation and using the fact that $\mathbf{V}_{qP} \cdot \nabla = d/dT$ we arrive at the ordinary differential equation

$$\frac{d}{dT}\left(\rho R_{qP}^2\right) = -\rho R_{qP}^2 \nabla \cdot \mathbf{V}_{qP}. \tag{38}$$

This provides an additional ordinary differential equation to solve in conjunction with equations (21) and (22).

2.4 Determination of the amplitude, phase, and trajectories

Given the current state of computing, there are a few ways that one may determine the amplitude, phase, and trajectories necessary for constructing a solution of the governing equation (6). The most direct way involves the numerical solution of equations (16) and (34) for both the slowness vector $\mathbf{p}$ and the amplitude vector $\mathbf{R}$. This involves solving two sets of nonlinear partial differential equations and can be challenging but there are a number of techniques that are available (Tadmor 2012, Bartels 2015). The nonlinearity of the equations is a reflection of the fact that several modes of propagation exist and must be determined at each point in medium. At boundaries or abrupt changes in velocity, the nature of the these modes may change. Note that, in adopting the form (7) with a real amplitude $\mathbf{R}(\mathbf{x},\omega)$ and phase $\varphi(\mathbf{x},\omega)$, we are neglecting decaying modes such as interface waves.

An alternative strategy is to solve the ordinary differential equations (21) and (22) in conjunction with the set that results from writing the partial differential equation (34) in ray coordinates. Such an approach has the added benefit of providing the trajectories $\mathbf{x}(s)$ as a direct bi-product of the solution. There are a wide range of numerical techniques for solving such systems (Cash and Carp 1990, Press et al. 2007, Ascher and Petzold 1998). However, the presence of the spatial derivatives contained in the gradients in the function $W(\mathbf{x},\omega)$ couples adjacent trajectories. Thus, one must solve for families of trajectories simultaneously or adopt a hybid grid- and trajectory-based approach (Wyatt 2005). The general methodology is akin to dynamic ray tracing (Cerveny et al. 1988, Gajewski and Psencik 1990) and the adoption of paraxial ray coordinates (Waheed Bin et al. 2013) in order to describe the propagating wavefront. One useful aspect of trajectories based upon equations (21) and (22) is that the paths do not cross and do not display singular behavior, leading to more stable numerics when tracing rays (Foreman 1989, Wyatt 2005).

A third possibility is to take advantage of the active development of numerical techniques, such as finite-differences or finite-elements (Fichtner 2011, Igel 2017), for the solution of the governing equation (4). This was the methodology taken by Foreman (1989) and Protasov and Gadylshin (2017) in their study of the Helmholtz equation. Going forward, this may well be the most popular approach for computing trajectories that are valid in general elastic models. In order to estimate the amplitude and phase one would post-process the results from a numerical simulation and decompose the solution into the polar form (7). Identification of the first arriving compressional mode is relatively straight-forward, given its distinct arrival time and early onset. Later arrivals are more difficult to identify clearly and require a phase separation algorithm, such as developed by Sun et al. (2004), Yan and Sava (2011), and Cheng and Fomel (2014). The trajectories follow from integrating equation (21) after determining $\mathbf{R}$ and φ and completing the eigen-decomposition (24). They also follow from travel times of a simulation and the determination of the group velocity vector field. In comparison to asymptotic ray theory and eikonal equation-based approaches, such trajectories provide a better representation of the propagation of a seismic disturbance for a narrow frequency band.

2.5 Travel times

A fundamental quantity in tomographic imaging is the propagation time of an elastic wave from a source to a given point in the Earth. An expression for the travel time along an extended trajectory follows directly from equation (21) if we consider the time that it takes for a wave to travel an incremental distance dl along the path. In particular, we have

$$\frac{dl}{dT} = \sqrt{\left(\frac{dx_1}{dT}\right)^2 + \left(\frac{dx_2}{dT}\right)^2 + \left(\frac{dx_3}{dT}\right)^2} = |\mathbf{V}| = V \tag{39}$$

where V is the magnitude of the group velocity vector $\mathbf{V}$. Therefore the travel time is given by

$$T = \int_{\mathbf{x}} \frac{1}{V} dl \tag{40}$$

where

$$V = \sqrt{\sum_{j=1}^{3} \left(\hat{\mathbf{R}}^t \mathbf{a}_{jm} \hat{\mathbf{R}} p_m\right)^2}. \tag{41}$$

This formulation is similar to that of asymptotic ray theory and forms the basis for imaging algorithms suited to an anisotropic medium [see for example Jech 1991, Chapman and Pratt 1992, Wu and Lees 1999, Brantut 2018]. It has been pointed out (Jech 1991) that the group velocity and slowness are nonlinear functions of both the properties of the medium as well as the direction of propagations, as is evident in equation (41). For the first arriving quasi-compressional wave, qP, the displacements are in the direction of the polarization vector $\mathbf{g}_{qP}$ and the traveltime is given by

$$T_{qP} = \int_{\mathbf{x}} \frac{1}{V_{qP}} dl \tag{42}$$

where the compressional velocity is

$$V_{qP} = \sqrt{\sum_{j=1}^{3} \left(\hat{\mathbf{g}}_{qP}^t \mathbf{a}_{jm} \hat{\mathbf{g}}_{qP} p_m\right)^2}. \tag{43}$$

It is also possible to express the travel time along the trajectory in terms of the phase velocity, as discussed by Chapman and Pratt (1992). This equation for the travel time also follows from equation (21) if we consider

$$\mathbf{p} \cdot \mathbf{V} = p_j \frac{dx_j}{dT} = \hat{\mathbf{R}}^t \mathbf{a}_{jm} \hat{\mathbf{R}} p_m p_j. \tag{44}$$

We can use the fact that the Hamiltonian is equal to 1 along the trajectory, and the definition of the Hamiltonian (17), to write equation (44) as

$$p_j \frac{dx_j}{dT} = 1 + W \tag{45}$$

and thus

$$dT = \frac{1}{1+W} p_j dx_j \tag{46}$$

where we are summing over the repeated index j. Using the definition (27) of the phase velocity v we may calculate the travel time by integrating equation (46) along the trajectory

$$T = \int_{\mathbf{x}} \frac{1}{v\,(1+W)} \hat{p}_j dx_j, \tag{47}$$

an alternative expression for the travel time that is very similar to the one found in conventional ray theory. The presence of W in this equation is the only difference from the expression for the travel time given by Chapman and Pratt (1992). Thus, as W is reduced in magnitude, the travel time approaches that of high-frequency asymptotic ray theory. Conversely, using equation (47) we can calculate the deviation of an asymptotic travel time from the more accurate estimate given here.

3 APPLICATIONS

Here we consider two applications that highlight the deviations from asymptotic ray theory that may arise from small-scale variations in elastic properties. For simplicity, the first case involves a simple layer embedded in a uniform background medium. We examine how the normalized function $W(\mathbf{x}, \omega)$ changes as the boundaries of the layer become sharper and approach step-like changes in properties. For the second case we utilize velocity variations from a well log to construct a field-based layered velocity model.

In both examples we will consider an anisotropic medium that is symmetric about a vertical rotational axis and use the parameterization introduced by Thomsen (1986). Thus, the material may be characterized by a compressional and a shear velocity, α_o and β_o, respectively, and three dimensionless parameters δ, ε, and γ. Following Chapman (2004, p. 130) we can write the non-zero components of the matrix of anisotropy parameters as

$$C_{33} = \rho {\alpha_o}^2 \tag{48}$$

$$C_{44} = \rho {\beta_o}^2, \tag{49}$$

$$C_{11} = (1 + 2\varepsilon)\, C_{33}, \tag{50}$$

$$C_{66} = (1 + 2\gamma)\, C_{44}, \tag{51}$$

and

$$C_{13} = \sqrt{2C_{33}\left(C_{33} - C_{44}\right)\delta + \left(C_{33} - C_{44}\right)^2} - C_{44}. \tag{52}$$

The elements of the matrices $\mathbf{c}_{jk}$ in the governing equation (6) are given in terms of the elements of the 6×6 matrix C_{mn}

$$\mathbf{c}_{11} = \begin{pmatrix} C_{11} & C_{16} & C_{15} \\ C_{16} & C_{66} & C_{56} \\ C_{15} & C_{56} & C_{55} \end{pmatrix}, \tag{53}$$

$$\mathbf{c}_{22} = \begin{pmatrix} C_{66} & C_{26} & C_{46} \\ C_{26} & C_{22} & C_{24} \\ C_{46} & C_{24} & C_{44} \end{pmatrix}, \tag{54}$$

$$\mathbf{c}_{33} = \begin{pmatrix} C_{55} & C_{45} & C_{35} \\ C_{45} & C_{44} & C_{34} \\ C_{35} & C_{34} & C_{33} \end{pmatrix}, \tag{55}$$

$$\mathbf{c}_{12} = \begin{pmatrix} C_{16} & C_{12} & C_{14} \\ C_{66} & C_{26} & C_{46} \\ C_{56} & C_{25} & C_{45} \end{pmatrix}, \tag{56}$$

$$\mathbf{c}_{23} = \begin{pmatrix} C_{56} & C_{46} & C_{36} \\ C_{25} & C_{24} & C_{23} \\ C_{45} & C_{44} & C_{34} \end{pmatrix}, \tag{57}$$

$$\mathbf{c}_{31} = \begin{pmatrix} C_{15} & C_{56} & C_{55} \\ C_{14} & C_{46} & C_{45} \\ C_{13} & C_{36} & C_{35} \end{pmatrix}, \tag{58}$$

where the other matrices are obtained through the use of the symmetry $\mathbf{c}_{kj} = \mathbf{c}_{jk}{}^t$ (Chapman 2004, p. 95).

3.1 Propagation across a layer and the condition for the validity of high-frequency asymptotic ray theory

Perhaps the most common form of abrupt velocity variation within the Earth is associated with layering. In this section we consider an isolated layer in order to study the deviations from high-frequency asymptotic ray theory as the layer boundaries becomes a sharp transition. The anisotropic layer is embedded in a uniform isotropic background. The background compressional velocity of the medium is 4000 m/s while the shear wave speed is 2353 m/s, and the density is 2500 kg/m^3. The depth variation is given by a superposition of arc-tangent functions

$$f(z) = 1 + \Delta\left\{\arctan\left[\sigma\left(z - z_{top}\right)\right] - \arctan\left[\sigma\left(z - z_{bot}\right)\right]\right\} \tag{59}$$

where Δ is the magnitude of the change in velocity and σ is a parameter that controls the length-scale of the transition from the background velocity to the layer velocity. Smaller values of σ indicate a wider transition while larger values correspond to a rapid jump in properties. The top and bottom of the layer are determined by z_{top} and z_{bot}, respectively. In Figure 1, we display two different transitions for a 16 m thick layer centered at a depth of 300 m. The values of the length-scale parameter σ used in the tests were 0.1 and 10.0. The variation in Thomsen parameters for the layer characterized by $\sigma = 10.0$ are plotted Figure 1b.

High-frequency asymptotic ray theory is a useful approximation to our frequency-dependent trajectories if we can neglect W in equation (17). That is, conventional ray theory is appropriate for the frequencies under consideration if the magnitude of the function $W(\mathbf{x}, \omega)$ for the quasi-compressional wave (qP), given by

$$W(\mathbf{x}, \omega) = \frac{1}{R_{qP}\rho\omega^2}\hat{\mathbf{R}}^t_{qP}\left[\frac{\partial}{\partial x_j}\left(\rho \mathbf{a}_{jk}\frac{\partial \mathbf{R}_{qP}}{\partial x_k}\right)\right], \tag{60}$$

arrived at in equation (16), is much smaller than 1. In order to calculate $W(\mathbf{x}, \omega)$ we used a numerical finite-difference code to obtain the amplitude field $\mathbf{R}_{qP}(\mathbf{x}, \omega)$ at the two frequencies 10 and 200 Hz. We use a first-order stress-velocity formulation of the system of governing equations, given by equation (4), and solve the discrete three-dimensional system using time-domain finite differences, implementing a leap-frog scheme on a staggered grid. The time derivatives are computed using a 2nd-order symplectic time integration scheme (De Basabe and Sen 2010, Ma et al. 2019). The space derivatives are computed to 8th-order accuracy with FD coefficients that have been optimized to minimize dispersion over the wavenumber spectrum. Absorbing boundaries are achieved through convolutional perfectly matching layer (CPML) absorbing boundaries.

A point pressure source with a sinusoidal source-time function, located at $(x, y, z) = (300m, 300m, -200m)$, was implemented in the numerical model. The medium extends from 0 to 600 m both the x and y directions, and down to -600 m in depth. Two of the pressure fields, generated by sinusoidal sources, are shown in Figure 2 for a medium containing a layer at a depth of 300 m. The boundaries of the layer were constructed using equation (59) with $\sigma = 10.0$. For these calculations the compressional and shear velocities of 4000 and 2353 m/s, respectively, were multiplied by the depth-varying factors shown in Figure 1 while the density was held constant and the other anisotropy parameters varied as shown in Figure 1b. The gradient of the properties and the wave field amplitude functions were computed numerically in three-dimensions using piecewise polynomial interpolating functions. In this example we consider the faster quasi-compressional (qP) phase and its associated group velocity field $\mathbf{V}_{qP}$. The magnitude of $W(\mathbf{x}, \omega)$ is plotted in Figure 3 for a layer with smoothly-varying boundaries, corresponding to $\sigma = 0.1$ (Figure 3a). In these plots values of W exceeding 1 indicate a significant deviation from the conventional eikonal equation. To avoid the steep gradients in the wave field amplitude near the source we plot a cross-section at a distance of 300 m from the source. For $\omega = 10$ Hz the magnitude of W is small throughout the vertical slice (Figure 3b). At the significantly higher frequency of 200 Hz the size of W is also much less than 1 throughout the volume. Thus, away from the source, asymptotic ray theory is a valid approximation, as expected for this smoothly-varying medium.

To determine the variations between conventional ray paths and the frequency-dependent rays, we computed the trajectories from the source to the receivers for the case shown in Figure 3, for which $\sigma = 0.1$. For the conventional ray paths a fast sweeping eikonal equation solver, generalized for a vertical transversely isotropic velocity, was used to calculate the quasi-compressional wave (qP) travel time field (Tsai et al. 2003, Qian et al. 2007). Using the approach of Brantut (2018) the phase velocity field was transformed into the group velocity field to compute the travel time field for

the group arrivals. The trajectories associated with the wave field are computed using equation (21) where $(\mathbf{V}_{qP})_i$ is the group velocity of the propagating quasi-compressional wavefront. The ordinary differential equations were solved using Heun's method, a modified Euler's method that is similar to a two-stage Runge-Kutta method (Leader 2004) and maintains a quadratic improvement in accuracy with decreasing step size. The approach improves upon the Euler estimate by first computing the dependent variable at an intermediate value and then using this for a final approximation of the update. For the problem defined by equation (21), say we are at a point $\mathbf{x}_n$ on the trajectory, corresponding to the position, distance or time, s_n on the path. The right-hand-side is denoted by the velocity vector field $\mathbf{V}_{qP}(\mathbf{x}_i, s_i)$ that is derived from the group velocity vector given by equation (43), obtained from the finite-difference simulation. The intermediate point $\bar{\mathbf{x}}_{i+1}$ is given by

$$\bar{\mathbf{x}}_{i+1} = \mathbf{x}_i + h\mathbf{V}_{qP}(\mathbf{x}_i, s_i) \tag{61}$$

and the next point along the trajectory is given by

$$\mathbf{x}_{i+1} = \mathbf{x}_i + \frac{h}{2}\left[\mathbf{V}_{qP}(\mathbf{x}_i, s_i) + \mathbf{V}_{qP}(\bar{\mathbf{x}}_{i+1}, s_{i+1})\right] \tag{62}$$

where h is the size of the step along the path and $s_{i+1} = s_i + h$. In Figure 4 we plot both the trajectories computed using a modified eikonal equation approach presented in Brantut (2018) and those computed using equations (61) and (62). For the smoothly-varying transition, shown in the Figure 3a, there is general agreement between the eikonal paths and the extended trajectories, as expected given the small value of $W(\mathbf{x}, \omega)$.

Increasing σ to 10.0 results in a layer bounded by rapidly-varying velocities [see Figures 1 and 5a]. In this case the presence of the layer clearly produces large values for the lower frequency of 10 Hz. Specifically, in Figure 5b we see that W exceeds 1 at the top edge of the layer where the amplitude of the wave field is large (Figure 2) and the velocity is varying rapidly with depth (Figure 5a). At the higher frequency of 200 Hz the absolute value of W is much less than 1 over the entire region (Figure 5c), likely due to the fact that ω^2 in the denominator is 400 times larger at this frequency. The sharp transitions at the edges of the layer also lead to differences between conventional raypaths based upon the eikonal equation and those derived from the wave field calculations (Figure 6). At the lower frequency of 10 Hz there are significant differences between the eikonal and extended trajectories for paths from the source to receivers located at or below a depth of 300 m. Increasing the dominant frequency to 200 Hz increases the concentration of these lowermost trajectories (Figure 6c), resulting in paths that more nearly resemble those produced by the eikonal equation. However there are still significant differences between the frequency-dependent paths and those of high-frequency asymptotic ray theory. Vasco and Nihei (2019) presented several other examples for isotropic velocity models containing half-spaces and layers.

3.2 A layered model derived from well logs

Sequences of sand and shale are a major source of both anisotropy and abrupt changes in velocity. As an example we consider variations in properties determined from a well log from a sedimentary basin (Figure 7a). The log has been smoothed using a moving average but large and rapid depth variations are evident for this well. Similarly, shear velocities were derived from shear sonic logs. The compressional and shear velocities represent the average vertical velocities. The anisotropy is specified by the three additional parameters $\delta = 0.01$, $\epsilon = 0.13$, and $\gamma = 0.26$ that are considered constant in the model. The log velocities were incorporated into the finite-difference grid with a spacing of 4 m in each direction. A vertical slice through the resulting compressional velocity model is shown in Figure 7b.

3.2.1 A comparison of raypaths

The finite-difference algorithm described in the previous sub-section was used to compute wave fields at 20 and 100 Hz for the anisotropic model shown in Figure 7. Snapshots of the wave fields, taken 0.75 s after the initiation of the source, are shown in Figure 8 for the two frequencies. The group arrival time was computed from the calculated first arrivals of the quasi-compressional phase. The velocity field $\mathbf{V}_{qP}(\mathbf{x}, s)$ denotes the group velocity field that governs the propagation of a transient pulse. The resulting travel time fields are shown in Figure 9. The trajectories, also calculated using Heun's method given by equations (61) and (62), are shown in Figures 8 and 9 for the wave fields at 15 and 100 Hz. In Figure 9 we also plot the trajectories calculated using the eikonal equation and the fast sweeping algorithm mentioned earlier. The frequency-dependent rays, particularly those in the upper portion of the crosswell region, differ significantly from conventional paths calculated using the eikonal equation (Figure 9). The extended trajectories do not appear to bend as much in response to thin high velocity layers. In order to characterize the impact of the anisotropy on the frequency-dependent ray paths we plot the trajectories for an isotropic and anisotropic model at a frequency of 20 Hz in Figure 10. We observed deviations, particularly for rays corresponding to propagation in a nearly horizontal direction, where the differences between the isotropic and anisotropic velocities are the largest.

3.2.2 Traveltime sensitivities

The frequency-dependent trajectories provide some insight into travel time sensitivities associated with propagating elastic wavefronts. The two main approaches for estimating arrival times are picking the initial onset of a pulse and waveform cross-correlation methods. The estimated travel times from these two techniques are likely to differ and their corresponding sensitivities are not necessarily equivalent. The initial onset or first break corresponds to a ray theoretical travel time. As in Vlaar (1968) it is possible to formulate all the equations of ray theory as the propagation of a discontinuity of some derivative of the displacement field without invoking explicit high frequency assumptions. The ray theoretical arrival time of the wavefront denotes arrival of this discontinuity and the initiation of a seismic disturbance. A cross-correlation arrival time is very different in nature and will be dominated by the peak of the pulse and sensitivity to scattered energy and distortions of the waveform. This difference is manifested in the minimal sensitivity along the

ray theoretical trajectory (Marquering et al. 1999). Neither estimate or sensitivity is incorrect, they are just suited to different aspects of the seismic disturbance and the particular observational technique. Similarly, the trajectories introduced in this paper correspond to the propagation of components of the wave field associated with a specific frequency. As an example, in Figure 11 we plot ten trajectories associated with a single source receiver pair, located in the model plotted in Figure 7. The ray paths define a region that is sensitive to the 10, 20, 30, 40, 50, 60, 70, 80, 90, and 100 Hz components of the wave front. The frequency-dependent trajectories allow one to decompose the wave field into narrow bands and to construct tomography images at a given set of frequencies. Alternatively, observations from a number of frequencies may be inverted together. Such a decomposition provides additional flexibility when conducting seismic imaging.

4 CONCLUSIONS

Using a polar decomposition, it is relatively straight-forward to develop equations describing frequency-dependent trajectories associated with the propagation of an elastic disturbance in an anisotropic medium. The expressions are not limited to the high-frequency component of the wave field and are valid for a medium with rapidly-varying properties. The approach does neglect exponentially decaying waves that are restricted to interfaces and, in its current form, is suited for the study of body waves such as the quasi-compressional wave (qP), and the quasi-shear waves (qS_v and qS_h). It should be possible to modify the method, by altering the polar form, in order to study the propagation of surface waves in a heterogeneous Earth.

The semi-analytic expression for the Hamiltonian provides explicit conditions for the validity of a high-frequency asymptotic approximation when modeling frequency-dependent wave propagation. That is, for values of $W(\mathbf{x}, \omega)$ of the order of 1, the neglected terms approach the magnitude of those retained in the asymptotic expression. We consider an example of a layer with sharp boundaries, finding that the asymptotic approximation deviations from wave field computations at the edges of the layer. At these locations the spatial gradients of the wave field and/or the velocity field are large. For a layer with boundaries that vary over tens of meters the asymptotic approximation breaks down at a frequency of 10 Hz.

Adopting a sufficiently high frequency, 200 Hz in our single layer examples, improves the situation, and reinstates the validity of the asymptotic approximation. However, in the Earth we expect boundaries that are quite abrupt and layers that may be rather thin. In an application that adopts velocity variations from a well log obtained from a sedimentary basin, we observe velocity variations over a wide range of scales and sharp jumps in values. A comparison between trajectories computed using the high-frequency asymptotic approximation and those from a finite-difference numerical wave field simulation highlights the dramatic differences that can occur for particular raypaths. Furthermore, the frequency-dependence of the trajectories is evident in this example.

ACKNOWLEDGMENTS

This material is based upon work supported by the U.S. Department of Energy, Office of Science, Office of Basic Energy Sciences, Chemical Sciences, Geosciences, and Biosciences Division under contract number DE-AC02-05- CH11231.

REFERENCES

Aki, K. and Richards, P. G. (2002) *Quantative Seismology*, University Science Books, Sausalito.

Ascher, U. M., and L. R. Petzold (1998). *Computer Methods for Ordinary Differential Equations and Differential-Algebraic Equations*, Society for Industrial and Applied Mathematics, Philadelphia.

Bartels, S. (2015) *Numerical Methods for Nonlinear Partial Differential Equations*, Springer, New York.

Benseny, A., Albareda, G., Sanz, A. S., Mompart, J., and Oriols, X. (2014). Applied Bohmian mechanics, *European Physics Journal*, **68**, 286-329.

Bohm, D. (1952). A suggested interpretation of the quantum theory in terms of 'hidden variables' I, *Physical Review*, **85**, 166-179.

Bohm, D. (1989). *Quantum Theory*, Dover, New York.

Brantut, N. (2018). Time-resolved tomography using acoustic emissions in the laboratory, and application to sandstone compaction, *Geophysical Journal International*, **213**, 2177-2192, https://doi.org/10.1093/gji/ggy068.

Carcione, J. M. (2014). *Wave Fields in Real Media: Theory and Numerical Simulation of Wave Propagation in Anisotropic, Anelastic, Porous, and Electromagnetic Media*, Elsevier Science, Amsterdam.

Cardarelli, E., and Cerreto, A. (2002). Ray tracing in elliptical anisotropic media using the linear traveltime interpolation (LTI) method applied to traveltime seismic tomography, *Geophysical Prospecting*, **50**, 55-72.

Cash, J. R., and A. H. Carp (1990). A variable order Runge-Kutta method for initial value problems with rapidly varying right-hand sides, *ACM Transactions on Mathematical Software*, **16**, 201-222.

Cerveny, V. (1972). Seismic rays and ray intensities in inhomogeneous anisotropic media, *Geophysical Journal of the Royal Astronomical Society*, **29**, 1-13.

Cerveny, V., and Soares, J. E. P. (1992). Fresnel volume ray tracing, *Geophysics*, **57**, 902-915.

Cerveny, V., Molotkov, I. A., and Psencik, I. (1977). *Ray Methods in Seismology*, Charles University Press, Praha.

Cerveny, V., Klimes, L., and Psencik, I. (1988). Applications of dynamic ray tracing, *Physics of the Earth and Planetary Interiors*, **51**, 25-35.

Chapman, C. H. (2004). *Fundamentals of Seismic Wave Propagation*, Cambridge University Press, Cambridge.

Chapman, C. H., and Pratt, R. G. (1992). Traveltime tomography in anisotropic media - I. Theory, *Geophysical Journal International*, **109**, 1-19.

Cheng, J., and Fomel, S. (2014). Fast algorithms for elastic-wave-mode separation and vector decomposition using low-rank approximation for anisotropic media, *Geophysics*, **79**, C97-C110.

Coates, R. T., and Chapman, C. H. (2007). Generalized Born scattering of elastic waves in 3-D media, *Geophysical Journal International*, **107**, 231-263.

Courant, R. and Hilbert, D. (1966). *Methods of Mathematical Physics*, John Wiley, New York.

De Basabe, J. D., and Sen, M. K. (2010). Stability of the high-order finite elements for acoustic or elastic wave propagation with high-order time stepping, *Geophysical Journal International*, **181**, 577-590.

Faria, E. L., and Stoffa, P. L. (1994). Finite-difference modeling in transversely isotropic media, *Geophysics*, **59**, 282-289.

Fichtner, A. (2011). *Full Seismic Waveform Modelling and Inversion*, Springer-Verlag, Berlin.

Foreman, T. L. (1989). An exact ray theoretical formulation of the Helmholtz equation, *Journal of the Acoustical Society of America*, **86**, 234-246.

Gajewski, D. and Psencik I. (1987). Computation of high-frequency seismic wavefields in 3-D laterally inhomogeneous anisotropic media, *Geophysical Journal of the Royal Astronomical Society*, **91**, 383-411.

Gajewski, D. and Psencik I. (1990). Vertical seismic profile synthetics by dynamic ray tracing in laterally varying layered anisotropic structures, *Journal of Geophysical Research*, **95**, 11301-11315.

Gou, T., Zhao, D., Huang, Z., and Wang, L. (2018). Anisotropic 3-D ray tracing and its application to Japan subduction zone, *Journal of Geophysical Research*, **123**, 4088-4108.

Grechka, V., Singh, P, and Das, I. (2011). Estimation of effective anisotropy simultaneously with locations of microseismic events, *Geophysics*, **76**, WC143-WC155.

Gu, B, and Garashchuk, S. (2016). Quantum dynamics with Gaussian bases defined by quantum trajectories, *Journal of Chemical Physics*, **120**, 3023-3031.

Igel, H. (2017). *Computational Seismology - A Practical Introduction*, Oxford University Press, Oxford.

Ishimaru, A. (1997). *Wave Propagation and Scattering in Random Media*, IEEE Press, New York.

Jech, J. (1991). Computation of elastic parameters of anisotropic medium from travel times of quasi-compressional waves, *Physics of the Earth and Planetary Interiors*, **66**, 153-159.

Kohler, M. D., Allam, A., Massari, A., and Lin, F.-C. (2018). Detection of building damage using Helmholtz tomography, *Bulletin of the Seismological Society of America*, **78**, 2062-2076.

Koroni, M., Paulssen, H., and Trampert, J. (2019). Sensitivity kernels of PP precursor traveltimes and their limitations for imaging topography of discontinuities, *Geophysical Research Letters*, **46**, 698-707.

Leader, J. J. (2004). *Numerical Analysis and Scientific Computation*, Addison-Wesley, Boston.

Li, J., Li, C., Morton, S. A., Dohmen, T., Katahara, K. and Toksoz, M. N. (2014). Microseismic joint location and anisotropic velocity inversion for hydraulic fracturing in a tight Bakken reservoir, *Geophysics*, **79**, C111-C122.

Lin, F.-C., and Ritzwoller, M. H. (2011). Helmholtz surface wave tomography for isotropic and aziumuthally anisotropic structure, *Geophysical Journal International*, **186**, 1104-1120.

Lomax, A. (1994). The wavelength-smoothing method for approximating broad-band propagation through complicated velocity structures, *Geophysical Journal International*, **117**, 313-334.

Luo, Y., (1991). Calculation of wavepaths for band-limited seismic waves, *61-st Annual Meeting, Society of Exploration Geophysicists*, 1509-1512.

Luo, Y., and Schuster, G. T. (1991). Wave-equation traveltime inversion, *Geophysics*, **56**, 645-653.

Ma, X., Li, Y., and Song, J. (2019). A stable auxiliary differential equation perfectly matched layer condition combined with low-dispersive symplectic methods for solving second order elastic wave equations, *Geophysics*, **84**, T193-T206.

Marquering, H., Dahlen, F. A., and Nolet, G. (1999). Three-dimensional sensitivity kernels for finite-frequency traveltimes: the banana-doughnut paradox, *Geophysical Journal International*, **137**, 805-815.

Mavko, G., Mukerji, T., and Godfrey, N. (1995). Predicting stress-induced velocity anisotropy in rocks, *Geophysics*, **60**, 1081-1087.

Nur, A. (1971). Effects of stress on velocity anisotropy in rocks with cracks, *Journal of Geophysical Research*, **76**, 2022-2034.

Orefice, R., Giovanelli, R., and Ditto, D. (2009). Complete Hamiltonian description of wave-like features in classical and quantum physics, *Foundations of Physics*, **39**, 256-272, doi 10.007/s10701-009-9280-2.

Press, W. H., S. A. Teukolsky, W. T. Vetterling, and B. P. Flannery (2007). *Numerical Recipes*, Cambridge University Press,

Cambridge.

Protasov, M., and Gadylshin, K. (2017). Computational method for exact frequency-dependent rays on the basis of the solution of the Helmholtz equation, *Geophysical Journal International*, **210**, 525-533, https://doi.org/10.1093/gji/ggx188.

Qian, J., Zhang, Y.-T., and Zhao, H.-K. (2007). A fast-sweeping method for static convex Hamilton-Jacobi equations, *Journal of Scientific Computing*, **31**, 237-271.

Robertsson, J. O. A., Blanch, J. O., Nihei, K., and Tromp, J. (2012). *Numerical Modeling of Seismic Wave Propagation: Gridded Two-Way Wave-Equation Methods*, Geophysical Reprint Series No. 28, Society of Exploration Geophysicists, Tulsa.

Sarkar, D., Bakulin, A., and Kranz, R. L. (2003). Anisotropic inversion of seismic data for stressed media: Theory and a physical modeling study of Berea Sandstone, *Geophysics*, **68**, 1-15.

Sato, H., Fehler, M. C., and Maeda, T. (2012). *Seismic Wave Propagation and Scattering in the Heterogeneous Earth*, Springer, Heidelberg.

Sayers, C. (2010). *Geophysics Under Stress: Geomechanical Applications of Seismic and Borehole Acoustic Waves*, 2010 Distinguished Instructor Short Course Series No. 13, Society of Exploration Geophysicists, Tulsa.

Sayers, C., and Kachanov, M. (1995). Microcrack-induced elastic wave anisotropy of brittle rocks, *Journal of Geophysical Research*, **100**, 4149-4156.

Sethian, J. A. (1999). *Level Set Methods and Fast Marching Methods*, Cambridge University Press, Cambridge.

Shearer, P. M., and Chapman, C. H. (1989). Ray tracing in azimuthally anisotropic media - I. Results of models of aligned cracks in the upper crust, *Geophysical Journal International*, **96**, 51-64.

Stark, P., and Nikolayev, D. I. (1993). Toward tubular tomography, *Journal of Geophysical Research*, **98**, 8095-8106.

Strang, G. (2016). *Introduction to Linear Algebra*, Wellesley-Cambridge Press, Wellesley.

Sun, R., McMechan, G., Hsiao, M. and Chow, J. (2004). Separating P- and S-waves in a prestack three-dimensional elastic seismogram by divergence and curl computations, *Geophysics*, **51**, 286-297.

Tadmor, E. (2012). A review of numerical methods for nonlinear partial differential equations, *Bulletin of the American Mathematical Society*, **49**, 507-554.

Takabayasi, T. (1952). On the formulation of quantum mechanics associated with classical pictures, *Progress in Theoretical Physics*, **8**, 143.

Tarantola, A. (1984). The seismic reflection inverse problem, in *Inverse Problems of Acoustic and Elastic Waves*, F. Santosa, Y., Pao, W. W. Symes, and C. Holland, (Eds.), Siam, Philadelphia.

Tarantola, A. (1988). Theoretical background for the inversion of seismic waveforms, including elasticity and attenuation, *Pure and Applied Geophysics*, **128**, 365-399.

Thomsen, L. (1986). Weak elastic anisotropy, *Geophysics*, **51**, 1954-1966.

Thurston, R. N., and Brugger, K. (1964). Third-order elastic constants and the velocity of small amplitude elastic waves in homogeneously stressed media, *Physical Review A*, **133**, 1604-1610.

Tsai, Y.-H.R., Cheng, L.-T., Osher, S., and Zhao, H.-K. (2003). Fast sweeping algorithms for a class of Hamilton-Jacobi equations, *SIAM Journal of Numerical Analysis*, **41**, 673-694.

Tsvankin, I. (2012). *Seismic Signatures and Analysis of Reflection Data in Anisotropic Media*, Society of Exploration Geophysicists, Tulsa.

Vasco, D. W. (2018). An extended trajectory mechanics approach for calculating the path of a pressure transient: Derivation and illustration, *Water Resources Research*, **54**, https://doi.org/10.1002/2017WR021360.

Vasco, D. W., and Nihei, K. (2019). Broad-band trajectory mechanics, *Geophysical Journal International*, **216**, 745-759, https://doi.org/10.1093/gji/ggy435.

Vasco, D. W., and Majer, E. L. (1993). Wavepath traveltime tomography, *Geophysical Journal International*, **115**, 1055-1069.

Vasco, D. W., Peterson, J. E., and Majer, E. L. (1995). Beyond ray tomography: Wavepaths and Fresnel volumes, *Geophysics*, **60**, 1790-1804.

Vavrycuk, V. (2001). Ray tracing in anisotropic media with singularities, *Geophysical Journal International*, **145**, 265-276.

Vlaar, N. J. (1968). Ray theory for an anisotropic inhomogeneous elastic medium, *Bulletin of the Seismological Society of America*, **58**, 2053-2072.

Waheed Bin, U., Psencik, I., Cerveny, V., Iversen, E., and Alkhalifah, T. (2013). Tow-point paraxial traveltime formula for inhomogeneous isotropic and anisotropic media: tests of accuracy, *Geophysics*, **78**, C41-C56.

Weilandt, E. (1987). On the validity of the ray approximation for interpreting delay times, in *Seismic Tomography with Applications in Global Seismology and Exploration Geophysics*, G. Nolet (Ed.), D. Reidel Publishing Company.

Woodhouse, J. H. (1974). Surface waves in laterally varying media, *Geophysical Journal of the Royal Astronomical Society*, **37**, 29-51.

Woodward, M. J. (1992). Wave-equation tomography, *Geophysics*, **57**, 15-26.

Wu, H., and Lees, J. M. (1999). Cartesian parameterization of anisotropic traveltime tomography, *Geophysical Journal International*, **137**, 64-80.

Wyatt, R. E. (2005). *Quantum Dynamics with Trajectories*, Springer, New York.

Yan, J., and Sava, P. (2011). Improving the efficiency of elastic wave-mode separation for heterogeneous tilted transverse isotropic media, *Geophysics*, **76**, T65-T78.

Zelt, C. A., and Chen, J. (2016). Frequency-dependent traveltime tomography for near-surface seismic refraction data, *Geophysical Journal International*, **207**, 72-88.

Zhang, M., Xu, T., Bai, Z., Youshan, L., Hou, J., and Yu, G. (2017). Ray tracing of turning wave in elliptically anisotropic media with and irregular surface, *Earthquake Science*, **30**, 219-228.

5 APPENDIX

In this Appendix we provide the steps required to obtain coupled equations describing the evolution of the amplitude $\mathbf{R}(\mathbf{x},\omega)$ and phase $\varphi(\mathbf{x},\omega)$ of a propagating elastic wave. We begin with the governing equation (6) which we restate here:

$$-\omega^2\rho\mathbf{U} = \frac{\partial}{\partial x_j}\left[\mathbf{c}_{jk}\frac{\partial \mathbf{U}}{\partial x_k}\right]. \qquad (A1)$$

First, we expand this equation by carrying out the differentiation of the quantity within the square brackets

$$-\omega^2\rho\mathbf{U} = \frac{\partial \mathbf{c}_{jk}}{\partial x_j}\frac{\partial \mathbf{U}}{\partial x_k} + \mathbf{c}_{jk}\frac{\partial^2 \mathbf{U}}{\partial x_j \partial x_k}. \qquad (A2)$$

Consider the polar representation of the propagating wave

$$\mathbf{U}(\mathbf{x},\omega) = \mathbf{R}(\mathbf{x},\omega)e^{i\varphi(\mathbf{x},\omega)} \qquad (A3)$$

and substitute it into equation (A2). Each term has a factor $e^{i\varphi}$ which we can divide out from both sides. The resulting expression is a complex equation

$$-\rho\omega^2\mathbf{R} = \frac{\partial \mathbf{c}_{jk}}{\partial x_j}\frac{\partial \mathbf{R}}{\partial x_k} + i\frac{\partial \mathbf{c}_{jk}}{\partial x_j}\mathbf{R}\frac{\partial \varphi}{\partial x_k} + \mathbf{c}_{jk}\frac{\partial^2 \mathbf{R}}{\partial x_j \partial x_k}$$

$$+i\mathbf{c}_{jk}\frac{\partial \mathbf{R}}{\partial x_k}\frac{\partial \varphi}{\partial x_j} + i\mathbf{c}_{jk}\frac{\partial \mathbf{R}}{\partial x_j}\frac{\partial \varphi}{\partial x_k} + i\mathbf{c}_{jk}\mathbf{R}\frac{\partial^2 \varphi}{\partial x_j \partial x_k}$$

$$-\mathbf{c}_{jk}\mathbf{R}\frac{\partial \varphi}{\partial x_k}\frac{\partial \varphi}{\partial x_j}, \qquad (A4)$$

that is equivalent to two equations, one where the real terms are set equal to zero and another equation only containing the imaginary terms. In the following two sub-section we consider each case in succession.

5.1 Real Terms

Collecting the real terms in equation (A4) leads to a coupled equation in $\mathbf{R}(\mathbf{x},\omega)$ and $\varphi(\mathbf{x},\omega)$

$$\rho\omega^2\mathbf{R} + \frac{\partial \mathbf{c}_{jk}}{\partial x_j}\frac{\partial \mathbf{R}}{\partial x_k} + \mathbf{c}_{jk}\frac{\partial^2 \mathbf{R}}{\partial x_j \partial x_k} - \mathbf{c}_{jk}\mathbf{R}\frac{\partial \varphi}{\partial x_k}\frac{\partial \varphi}{\partial x_j} = 0. \qquad (A5)$$

Rearranging the terms in this expression, combining those containing partial derivatives in $\mathbf{R}$ by pulling out the derivative with respect to $\mathbf{x}_j$, and introducing the identity matrix $\mathbf{I}$ results in

$$\left[\mathbf{c}_{jk}\frac{\partial \varphi}{\partial x_k}\frac{\partial \varphi}{\partial x_j} - \rho\omega^2\mathbf{I}\right]\mathbf{R} = \frac{\partial}{\partial x_j}\left(\mathbf{c}_{jk}\frac{\partial \mathbf{R}}{\partial x_k}\right). \qquad (A6)$$

Note that if the right-hand-side could be neglected, equation (A6) would reduce to an expression that appears in high-frequency asymptotic approximations (Chapman 2004, p. 164). In that case the amplitude and phase decouple and equation (A6) could be solved directly for φ.

5.2 Imaginary Terms

Now consider the expression that results when we set the sum of the imaginary terms in equation (A4) to zero,

$$\frac{\partial \mathbf{c}_{jk}}{\partial x_j}\mathbf{R}\frac{\partial \varphi}{\partial x_k} + \mathbf{c}_{jk}\frac{\partial \mathbf{R}}{\partial x_k}\frac{\partial \varphi}{\partial x_j} + \mathbf{c}_{jk}\frac{\partial \mathbf{R}}{\partial x_j}\frac{\partial \varphi}{\partial x_k} + \mathbf{c}_{jk}\mathbf{R}\frac{\partial^2 \varphi}{\partial x_j \partial x_k} = 0. \qquad (A7)$$

Rearranging and grouping terms gives a second partial differential equation

$$\frac{\partial}{\partial x_j}\left[\frac{\partial \varphi}{\partial x_k}\mathbf{c}_{jk}\mathbf{R}\right] + \frac{\partial \varphi}{\partial x_j}\mathbf{c}_{jk}\frac{\partial \mathbf{R}}{\partial x_k} = 0 \qquad (A8)$$

that may be used to find the amplitude and phase of a propagating wave.

The terms in equations (A6) and (A8) resemble the partial differential described in Cerveny (1972) and those introduced by Chapman (2004, p. 164). In particular, the left-hand-side of equation (A6) is close to the Cerveny' (1972) N operator, while the right-hand-side is similar to the L operator. The M operator of Cerveny (1972) shares characteristics with the imaginary terms in equation (A8) and, as shown in Chapman (2004, p. 171), can be used to derive the transport equation.

Figure Captions

Figure 1. (a) Multiplication factors defining two layers with boundaries of varying sharpness. The layer boundaries are characterized by a function of the form given in equation (59). The parameter σ determines the width of the transition for the layer boundaries and smaller values of σ signify smoother edges. (b) Thomsen anisotropy parameters corresponding to the layer with sharp boundaries (σ=10.0).

Figure 2. Two vertical cross-sections through finite-difference simulations of elastic wave propagation through a medium containing a layer described by equation (59) with $\sigma = 10.0$ The pressure source, located at $(x, y, z) = (300m, 300m, -200m)$, has a one-sided sinusoidal source-time function. The two snapshots display the quasi-compressional wave fields (qP) associated with sinusoidal sources at two frequencies: (a) 10 Hz and (b) 200 Hz.

Figure 3. (a) Vertical cross-section through the compressional velocity model. The velocity model is smoothly-varying, corresponding to a value of $\sigma = 0.1$ in the expression (59), describing the vertical variation. The cross-section passes through the source location $(x, y, z) = (300m, 300m, -200m)$. (b) The magnitude of the function $W(\mathbf{x}, \omega)$ for a frequency of 10 Hz. (c) The magnitude of the function $W(\mathbf{x}, \omega)$ for a frequency of 200 Hz.

Figure 4. Trajectories associated with elastic quasi-compressional wave propagation through the model shown in Figure 3. The background colors in each panel indicate the traveltime fields, T_{qP}, corresponding to each calculation. (a) Trajectories calculated using the eikonal equation, (b) Paths for a source frequency of 10 Hz, calculated using the trajectory mechanics approach. (c) The paths for a 200 Hz sinusoidal source.

Figure 5. (a) The compressional velocities generated using a value of $\sigma = 10.0$ in equation (59). Magnitude of the scalar function $W(\mathbf{x}, \omega)$ given by equation (59) for two frequencies: 10 Hz (b) and 200 Hz (c).

Figure 6. (a) Trajectories associated with the propagation of quasi-compressional waves (qP), calculated using both the conventional high-frequency ray paths based upon the eikonal equation. Rays computed using the frequency-dependent extended trajectories based upon equation (21), (61), and (62). Two cases are plotted, corresponding to wavefields at 10 Hz (b) and 200 Hz (c).

Figure 7. (a) Compressional velocity variations as a function of depth, obtained from a well log from a sedimentary basin. (b) Vertical cross-section through the compressional velocity variation within a three-dimensional finite-difference grid used for the numerical solution of the eikonal equation and for wavefield simulation.

Figure 8. Two vertical cross-sections through two finite-difference simulations of quasi-compressional elastic wave propagation through the model shown in Figure 7. The pressure source, located at $(x, y, z) = (300m, 300m, -2300m)$, has a one-sided sinusoidal source-time function. The two simulations correspond to sinusoidal sources at two distinct frequencies (a) 20 Hz and (b) 100 Hz. The trajectories corresponding to each simulation are plotted as solid lines.

Figure 9. Quasi-compressional traveltimes and trajectories obtained by back-propagation from the receivers to the source using the group velocity field. That is, using equations (61) and (62) to calculate the path $\mathbf{x}(s)$ from the receivers to the sources, where $\mathbf{V}_{qP}(\mathbf{x}, s)$ is the group velocity field. The dashed lines correspond to the trajectories calculated using the eikonal equation while the solid lines are the extended trajectories.

Figure 10. Extended trajectories for isotropic (dashed) and anisotropic (solid) velocity models.

Figure 11. Extended trajectories for quasi-compressional wave propagation at 10, 20, 30, 40, 50, 60, 70, 80, 90, and 100 Hz with a source at (200, 300, -2300) and a receiver at (500, 300, -2300).

Figures

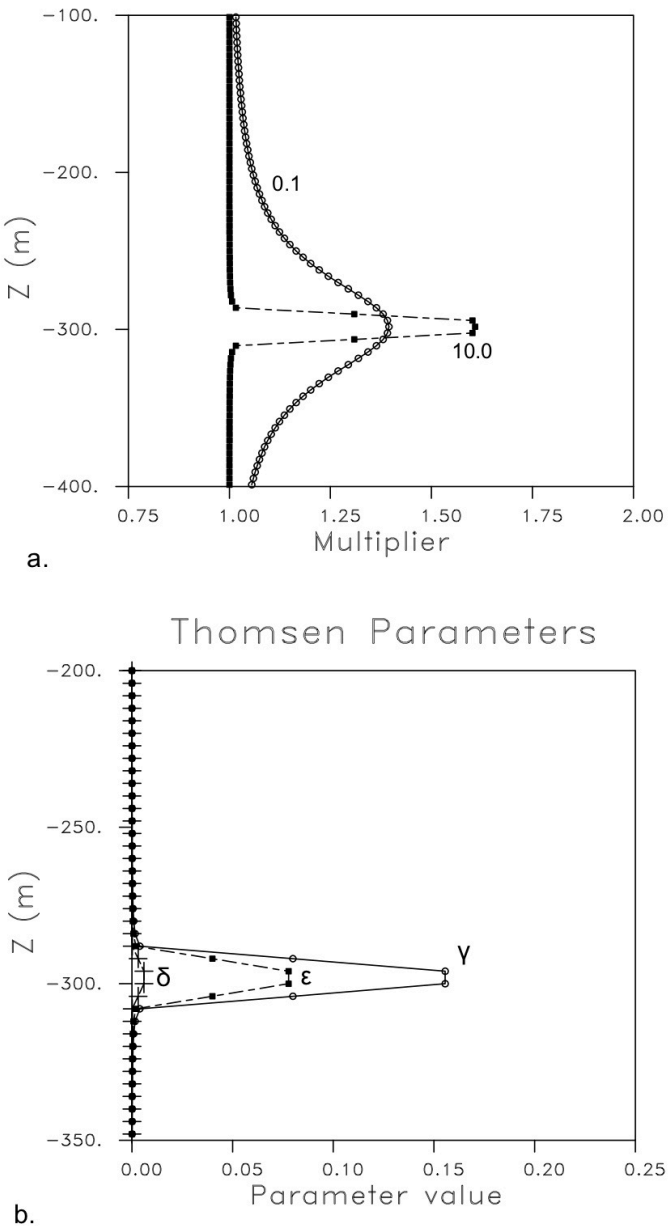

Figure 1. (a) Multiplication factors defining two layers with boundaries of varying sharpness. The layer boundaries are characterized by a function of the form given in equation (55). The parameter σ determines the width of the transition for the layer boundaries and smaller values of σ signify smoother edges. (b) Thomsen anisotropy parameters corresponding to the layer with sharp boundaries (σ=10.0).

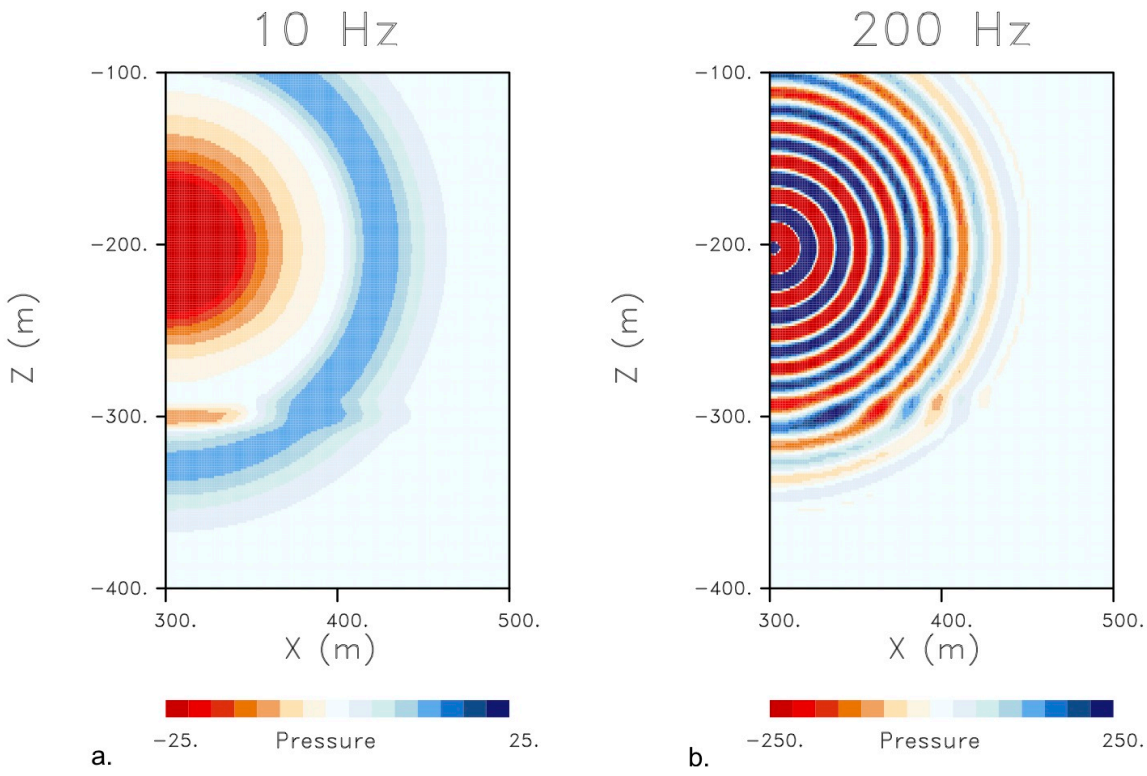

Figure 2. Two vertical cross-sections through finite-difference simulations of elastic wave propagation through a medium containing a layer described by equation (55) with $\sigma = 10.0$ The pressure source, located at $(x, y, z) = (300m, 300m, -200m)$, has a one-sided sinusoidal source-time function. The two snapshots display the quasi-compressional wave fields (qP) associated with sinusoidal sources at two frequencies: (a) 10 Hz and (b) 200 Hz.

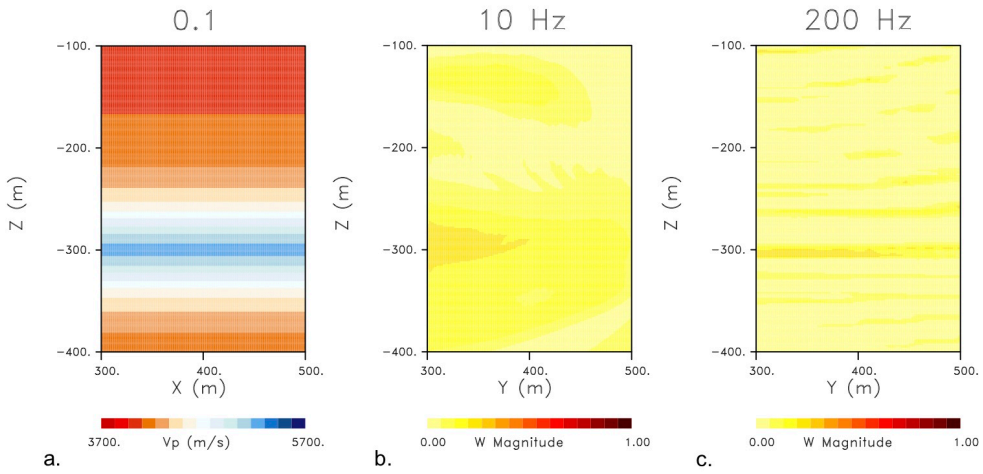

Figure 3. (a) Vertical cross-section through the compressional velocity model. The velocity model is smoothly-varying, corresponding to a value of $\sigma = 0.1$ in the expression (55), describing the vertical variation. The cross-section passes through the source location $(x, y, z) = (300m, 300m, -200m)$. (b) The magnitude of the function $W(\mathbf{x}, \omega)$ for a frequency of 10 Hz. (c) The magnitude of the function $W(\mathbf{x}, \omega)$ for a frequency of 200 Hz.

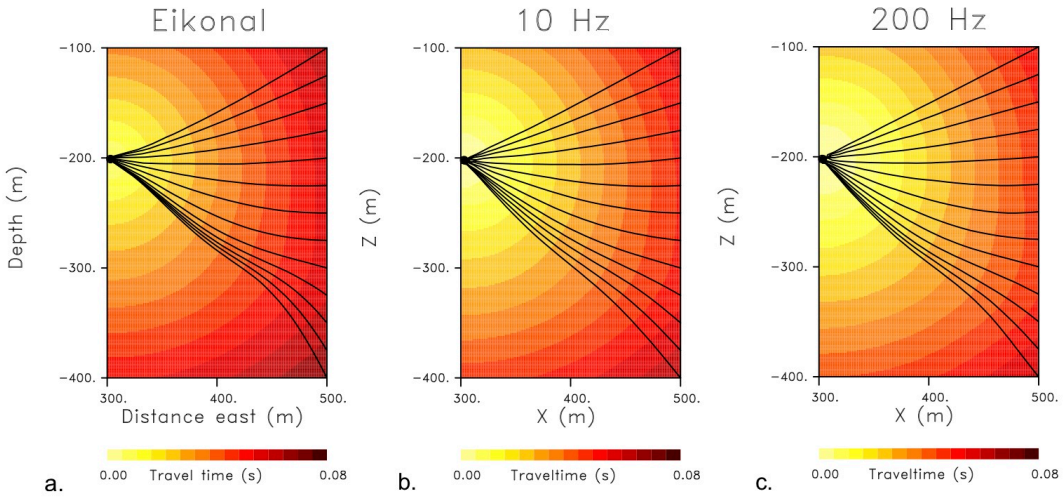

Figure 4. Trajectories associated with elastic quasi-compressional wave propagation through the model shown in Figure 3. The background colors in each panel indicate the traveltime fields, T_{qP}, corresponding to each calculation. (a) Trajectories calculated using the eikonal equation, (b) Paths for a source frequency of 10 Hz, calculated using the trajectory mechanics approach. (c) The paths for a 200 Hz sinusoidal source.

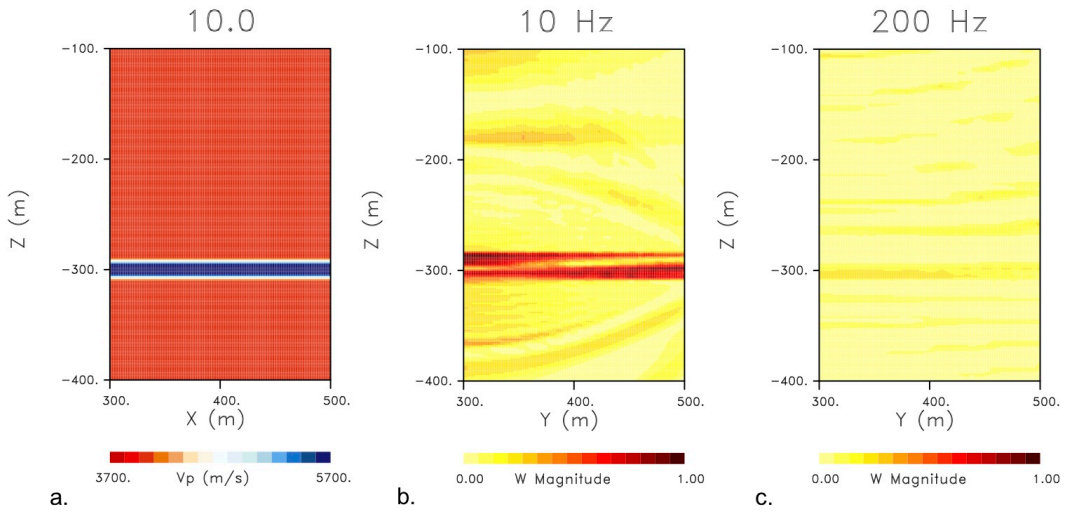

Figure 5. (a) The compressional velocities generated using a value of $\sigma = 10.0$ in equation (55). Magnitude of the scalar function $W(\mathbf{x}, \omega)$ given by equation (55) for two frequencies: 10 Hz (b) and 200 Hz (c).

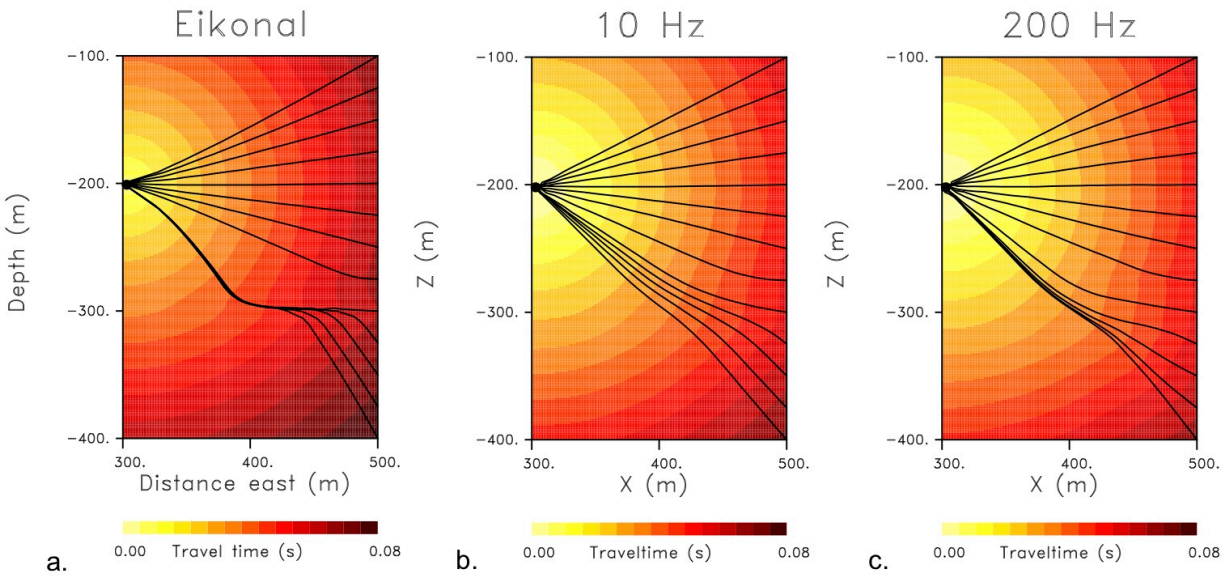

Figure 6. (a) Trajectories associated with the propagation of quasi-compressional waves (qP), calculated using both the conventional high-frequency ray paths based upon the eikonal equation. Rays computed using the frequency-dependent extended trajectories based upon equation (21), (57), and (58). Two cases are plotted, corresponding to wavefields at 10 Hz (b) and 200 Hz (c).

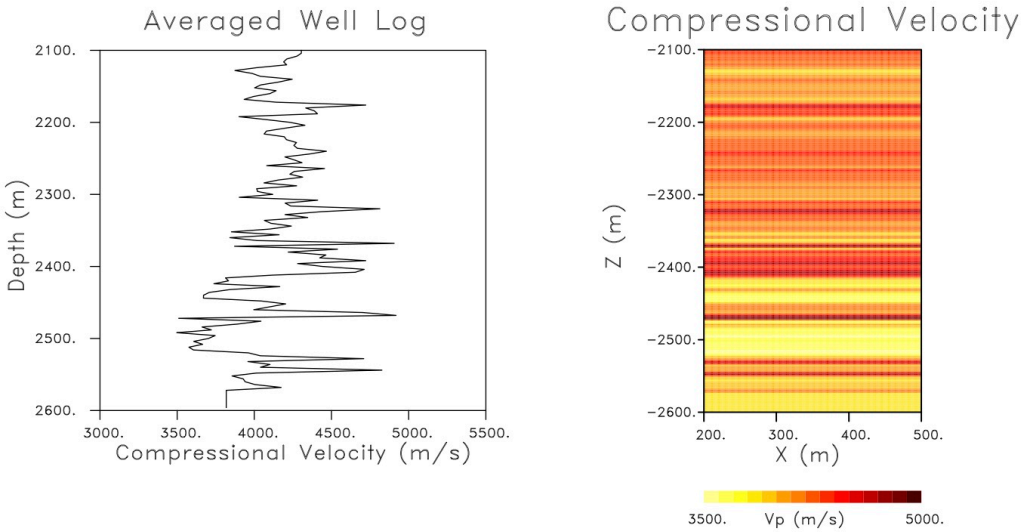

Figure 7. (a) Compressional velocity variations as a function of depth, obtained from a well log from a sedimentary basin. (b) Vertical cross-section through the compressional velocity variation within a three-dimensional finite-difference grid used for the numerical solution of the eikonal equation and for wavefield simulation.

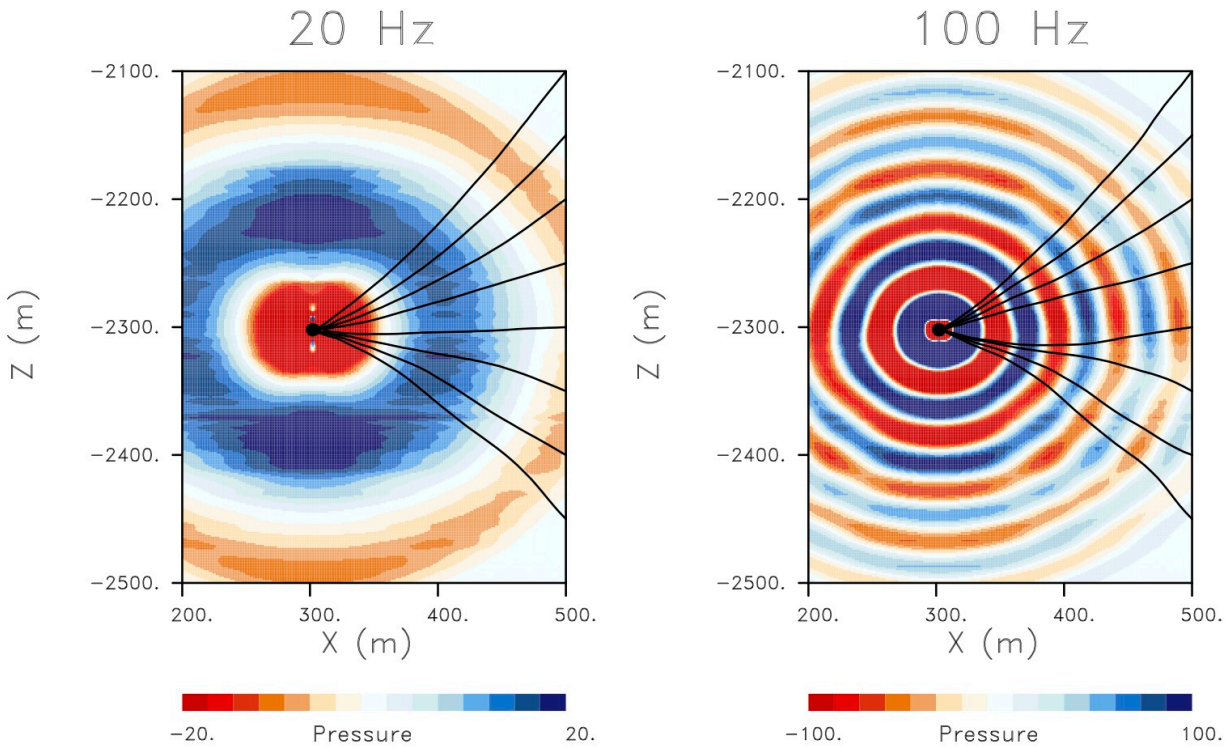

Figure 8. Two vertical cross-sections through two finite-difference simulations of quasi-compressional elastic wave propagation through the model shown in Figure 7. The pressure source, located at $(x, y, z) = (300m, 300m, -2300m)$, has a one-sided sinusoidal source-time function. The two simulations correspond to sinusoidal sources at two distinct frequencies (a) 20 Hz and (b) 100 Hz. The trajectories corresponding to each simulation are plotted as solid lines.

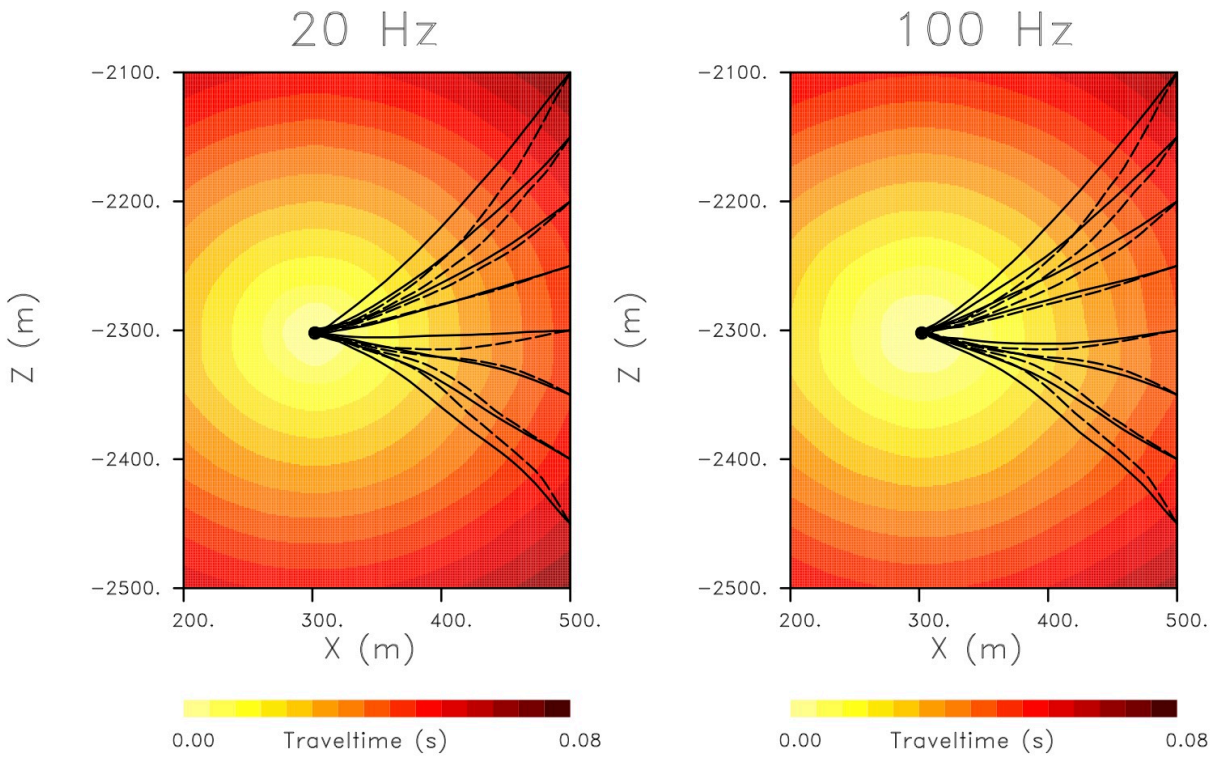

Figure 9. Quasi-compressional traveltimes and trajectories obtained by back-propagation from the receivers to the source using the group velocity field. That is, using equations (57) and (58) to calculate the path $\mathbf{x}(s)$ from the receivers to the sources, where $\mathbf{V}_{qP}(\mathbf{x}, s)$ is the group velocity field. The dashed lines correspond to the trajectories calculated using the eikonal equation while the solid lines are the extended trajectories.

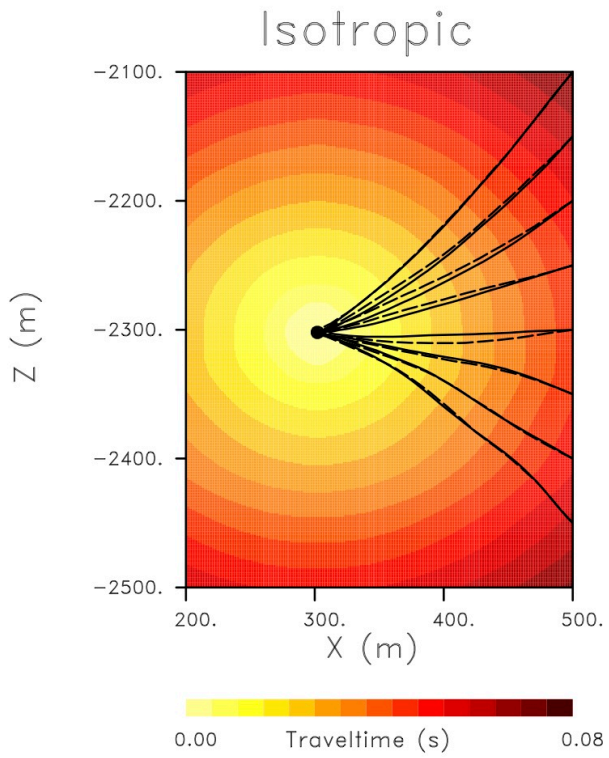

Figure 10. Extended trajectories for isotropic (dashed) and anisotropic (solid) velocity models.

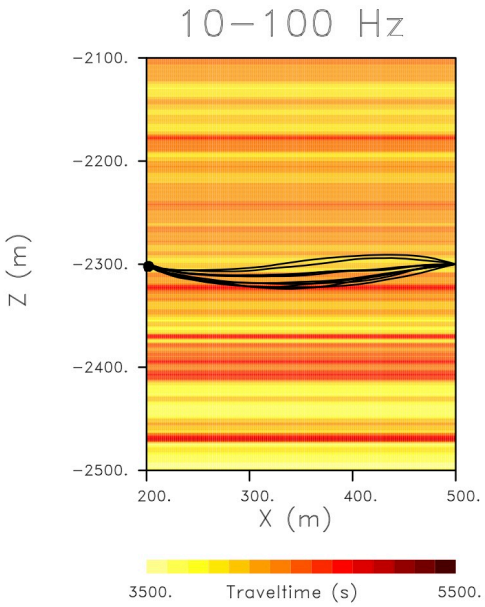

Figure 11. Extended trajectories for quasi-compressional wave propagation at 10, 20, 30, 40, 50, 60, 70, 80, 90, and 100 Hz with a source at (200, 300, -2300) and a receiver at (500, 300, -2300).